Signatures of Asymmetry in Neutron Spectra and Images Predicted by 3D Radiation Hydrodynamics Simulations of Indirect Drive Implosions.

J.P. Chittenden[a)], B.D. Appelbe, F. Manke[b)], K. McGlinchey, N.P.L. Niasse.

Centre for Inertial Fusion Studies, The Blackett Laboratory, Imperial College, London SW7 2AZ.

a) Electronic mail: j.chittenden@imperial.ac.uk

b) Presently at: Ecole Polytechnique Fédérale de Lausanne (EPFL), CH-1015 Lausanne, Switzerland

ABSTRACT

We present the results of 3D simulations of indirect drive inertial confinement fusion capsules driven by the 'High-Foot' radiation pulse on the National Ignition Facility (NIF). The results are post-processed using a semi-deterministic ray tracing model to generate synthetic DT and DD neutron spectra as well as primary and down scattered neutron images. Results with low-mode asymmetries are used to estimate the magnitude of anisotropy in the neutron spectra shift, width and shape. Comparisons of primary and down scattered images highlight the lack of alignment between the neutron sources, scatter sites and detector plane, which limits the ability to infer the ρr of the fuel from a down scattered ratio. Further calculations use high bandwidth multi-mode perturbations to induce multiple short scale length flows in the hotspot. The results indicate that the effect of fluid velocity is to produce a DT neutron spectrum with an apparently higher temperature than that inferred from the DD spectrum and which is also higher than the temperature implied by the DT to DD yield ratio.

I. INTRODUCTION

Non-uniformity in the radiation intensity reaching the surface of an indirect drive, inertial confinement fusion (ICF) capsule can result in strong variations in the areal density and velocity of the dense fuel layer converging on the axis. In addition, perturbations arising from the capsule mounting structure or from surface defects are amplified through Richtmyer-Meshkov and Rayleigh-Taylor instabilities during ablation and implosion and imprint upon the dense fuel layer during the deceleration phase. Such asymmetries can mean that not all of the momentum of the dense fuel is extinguished at stagnation and thus there is a reduction in the efficiency with which the kinetic energy is thermalized and hence a reduction in the pressure of the hotspot material[1,2,3,4,5]. Inhomogeneity in the dense fuel layer means that there are weak points of low inertia where the hotspot is not well confined. This promotes mixing of the cold fuel with the hotspot as well as an increase in hotspot surface area which boosts the thermal conduction losses[3] and truncates the burn duration[2].

One of the principal diagnostic approaches to understanding the role of asymmetry during the ICF stagnation phase is the use of neutron spectroscopy and imaging[6,7,8,9]. Images of the primary neutrons arising from DT reactions reflect the structure of the hotspot material, whereas images of neutrons down scattered to lower energies reveal the structure of the dense fuel layer surrounding the hotspot. For a stationary hotspot, the DT and DD neutron energy spectra are approximately Gaussian in shape, with a Doppler width governed by the Maxwellian distribution of ion velocities which can be used to estimate the ion temperature. Where asymmetry introduces a bulk fluid flow into the hotspot, however, this results in a Doppler shift of the thermonuclear neutron spectrum that is emitted[10]. Coherent motion of the hotspot material, as might be expected from a low-mode asymmetry, then induces a measurable anisotropy to the neutron spectra[11]. Where the component of fluid motion parallel to the line of sight to the detector is not the same at all points in the hotspot, then the variance of this velocity component broadens the Doppler width of the neutron pulse, giving a false signature of high apparent ion temperatures[12,2,13,14]. The sensitivity of neutron spectra to both the ion temperature and the fluid velocity represents both a diagnostic opportunity as well as a significant challenge when it comes to isolating the separate contributions.

In this work, we seek to evaluate whether signatures of different forms of bulk residual motion are embedded within synthetic neutron diagnostics. In section II, we describe the Chimera 3D radiation hydrodynamics model which is used to simulate a NIF capsule driven by the 'High-Foot' radiation pulse. A two phase approach to simulations is adopted where high resolution 1D calculations of the ablation phase (described in section III) are used to initialise 3D calculations of the deceleration and stagnation phase (described in section IV). Section V then describes a semi-deterministic approach to the generation of synthetic neutron spectra and images in post processing calculations. These models are then applied in section VI to calculate the effect of low mode asymmetries characterised by the Legendre polynomials P_0, P_1, P_2 and P_4 on neutron diagnostic signatures. Section VII then assesses the effects of shorter scale length motion in the hotspot using a high bandwidth multi-mode perturbation method. Finally in section VIII, we assess whether these synthetic neutron diagnostics signatures provide a qualitative comparison to the observed trends in NIF data.

The intention of these calculations is not to provide an accurate prediction of experiments on NIF, but rather to provide a means of understanding what neutron diagnostic signatures might tell us about the behaviour of the hotspot and dense fuel. A number of approximations are used in the radiation hydrodynamics simulations and in the construction of synthetic diagnostics. Where such approximations have been employed we have endeavoured to point them out.

II. THE CHIMERA RADIATION HYDRODYNAMICS CODE

Chimera is a 3D radiation hydrodynamics code recently developed at Imperial College. The model uses an Eulerian mesh in either Cartesian (x,y,z), cylindrical (r,z,θ) or spherical (r,θ,ϕ) geometry. Chimera utilises a fully explicit solution method, which maximises the scalability of the algorithm to large scale parallel computing by avoiding the matrix inversion techniques involved in implicit solutions. Hydrodynamic motion is solved using a 2nd order van Leer advection algorithm[15,16] together with a von Neumann-Richtmyer artificial viscosity. Ablator and fuel materials are advected separately with an approximate interface maintained using a SLIC[17] based method. Separate electron and ion energy equations are solved using tabulated equation of state data for energy densities, pressures, sound speed and ionic charge, for each material, which are calculated offline using the Frankfurt Equation of State (FEoS) model [18,19,20].

Electron and ion thermal conductivities, as well as equilibration rates, are calculated using the Epperlein-Haines modifications[21] to the Braginskii formulae[22]. Explicit solution of the thermal conduction equation requires sub-cycling using smaller time steps than the hydrodynamics algorithm, in order to retain numerical stability. For the electron thermal conduction a flux limiter of 0.04-0.06 is used. Where the flux limiter is invoked, the heat flow is solved as an advection equation with a time step determined by a Courant–Friedrichs–Lewy stability criterion which is far larger than that required for a stable solution of the diffusion equation and is only a factor of a few less than the hydrodynamics time step. The energy transfer through ion thermal conduction is generally much less than through the electrons. A notable exception is the first shock which propagates through the gas, where the gradient in ion temperature is substantial and may necessitate sub cycling and flux limiting of the ion heat flow.

Radiative energy transfer is modelled using an explicit solution[23] for the radiative flux and energy density based on the $P_{1/3}$ approximation[24] with the Automatic Flux Limiting[25,26] method used for the time integration of the radiation flux. Numerical stability for the explicit solution requires the speed of light transit across a computational cell to be resolved. The radiative transfer equations can however be modified to allow a reduced speed of light to be used and hence a larger time step. Provided that the speed of radiative energy transfer remains far faster than the characteristic hydrodynamics timescale, i.e. the reduced speed of light does not fall below c/10 and a minimum level of sub cycling is always observed, there is no observable change in the dynamics compared to using the full speed of light. For indirect drive using broad band X-ray sources, the penetration depth of the X-rays into the ablator material is a strong function of the X-ray energy and the frequency dependent opacity of the ablator material. In order to resolve these effects a multi-group approach is adopted where the radiative transfer solution is replicated for, in this case, 38 separate X-ray energy groups using average emissivities and opacities for each group as functions of density and temperature calculated offline using the Spk atomic physics code[27].

The Spk code is a Detailed Configuration Accounting (DCA) atomic solver which uses energy levels calculated from the Screened Hydrogenic Model (SHM) including n-l splitting (see Faussurier et al.[28]) which are augmented with experimental energy levels from the NIST database[29]. Level populations are solved using an extension to the Saha equation following the approach of effective temperatures developed by Busquet et al[30]. This provides a rapid method for calculating state populations in plasmas in collisional radiative equilibrium. For this work however the radiation field is more strongly coupled to the plasma temperature and an LTE approximation is therefore adopted. The method has been extended to include modifications to the effective temperature which take into account the effect of pressure ionization. This together with the addition of Compton and Thompson scattering provides a more accurate representation of opacity in cold, dense material. Detailed line profiles are calculated using a Voigt profile from the convolution of a Gaussian contribution from Doppler broadening with a Lorentzian contribution from the natural line width as well as the Stark broadening determined by the electron density. Much of this spectral detail is lost when generating average opacities for multi-group opacity tables, however retaining this level of spectral detail in the original calculation is essential in order to obtain accurate average opacities for each group. For simplicity we do not include here the contribution to opacity from silicon dopant layers in the capsule which are designed to eliminate high energy photons originating from M-band transitions in the gold hohlraum walls. Instead a purely black body spectrum is assumed so that the high energy photon component is reduced and the cold ablator opacity is then sufficient to prevent the early penetration of the radiation energy through the ablator into the fuel.

III. ABLATION AND IMPLOSION PHASE CALCULATIONS IN 1D

The capsule parameters and radiation temperature history used in simulations are based on NIF shot N130927 which is a representative example of the 'High-Foot' radiation pulse designs[31]. The capsule has an outer radius of 1.1315 mm, a 195 µm thick CH ablator and a 71.4 µm thick DT ice layer. Figure 1 shows the density as a function of radius and time from a 1D Chimera simulation of N130927, run in spherical geometry with a fixed uniform grid of 250 nm spatial resolution. Between 3 ns and 8.5 ns the radiation intensity of the 'trough' part of the drive pulse is relatively constant and a steady blow off from the surface of the ablator occurs launching the first shock at almost constant velocity through the ablator and into the ice layer. At 9 ns the intensity increases, launching a faster second shock which catches and merges with the first shock as they reach the inside surface of the ice layer. This reduces disassembly of the ice layer prior to its acceleration and thereby minimises the adiabat of the fuel[32].

Figure 2a indicates the loss of spectral resolution between the detailed opacity obtained from the Spk model and the group averaged opacity used in the Chimera calculations for a density and temperature indicative of the blow off plasma during the trough phase. Figure 2b illustrates how the dependence of the opacity on photon energy determines the penetration depth of the radiation in different energy groups, with a general trend to greater penetration for higher photon energies, but with strong absorption in the He and H-like carbon K-alpha lines and Li, He and H-like carbon K-alpha recombination edges giving rise to finite energy absorption in the lower density blow off plasma. Similarly, radiative energy is absorbed throughout a thicker ablation surface using a multi-group model compared to a single group radiation transport and results in a reduced density gradient.

IV. 3D SIMULATIONS OF LOW MODE RADIATION DRIVE ASYMMETRY

In this section we use simulations to calculate the form of hotspot structures and flows which arise from low mode asymmetry in the radiation drive, using Legendre polynomials as examples of perturbations which are cylindrically symmetric about the hohlraum axis. Rather than exploit this cylindrical symmetry, we simulate these effects using the full volume 3D Cartesian version of Chimera in order to be able to directly compare results to the higher mode asymmetric perturbations cases described in section VII. In principle these calculations could be performed by modelling the ablation phase for the entire capsule in 3D Cartesian geometry with an asymmetric radiation temperature source. In practice, such a calculation is not only time consuming but over convergences of 25 or more will retain a residual grid imprint superimposed on the effects of the Legendre polynomial.

Here we circumvent these issues by using the results of 1D calculations to reconstruct the approximate structure in 3D at a convergence level of 2.5:1 where the fuel has reached peak implosion velocity. By applying constant drive multipliers to the radiation pulse $T_r(t)$ in the range -4.5% to +4.5% in steps of 0.5% we generate a database of 1D results for different intensities. The plasma parameters at each point in the 3D Cartesian grid are then constructed by using the Legendre polynomial to determine the surface intensity and then interpolating between different 1D radial profiles. This method is only approximate as it neglects any transverse flow of material during the ablation and acceleration phases as well as the effects of any time dependence to the radiation drive asymmetry. From peak velocity onwards the fuel is coasting towards the axis and is hydrodynamically decoupled from the ablation region. The drive intensity is also past its peak and ablation plays little further role in the dynamics. This allows a simple radiation loss model based upon a probability of escape to be used during the stagnation phase, which expedites the 3D simulations. As a test, the 1D results shown above with 250nm resolution can be compared to 1D results with a simple radiation loss model used from peak velocity onwards. In addition these high resolution results can be compared to a lower (1μm) resolution 1D simulation initialised from the 250nm result at peak velocity as well as a similarly initialised 3D simulation of an unperturbed (P_0) capsule using a 1μm cubic Cartesian grid. Using neutron yield as a measure of integrated performance shows differences at the ~10% level ($1.05\text{x}10^{16}$, $1.08\text{x}10^{16}$, $9.6\text{x}10^{15}$, $9.5\text{x}10^{15}$ respectively) between these four calculations. Inspection of the density and temperature profiles throughout stagnation showed similar levels of consistency.

Figure 3 shows density slices through the mid plane of 3D Cartesian simulations using 1μm cubic grids for the unperturbed (P_0) case and for P_1, P_2 and P_4 perturbations applied. In each case the hohlraum axis is vertical. Here the variations in Tr(t) are determined by multiplying each Legendre polynomial by 0.03, i.e. there is a -3% to +3% variation in Tr(t) for the P_1, -3% to +1.5% for the P_2 and -3% to +1.2% for the P_4. The P_1 perturbation is equivalent to a vertical displacement of the capsule in the hohlraum and gives rise to a build-up of cold fuel above the hotspot forming a dense jet which penetrates through the centre of the hotspot. The centre of the hotspot is pushed downwards by a jet of cold fuel, eventually breaking through the reduced ρr at the bottom and into the residual ablator. The positive (prolate) P_2 perturbation equates to a high T_r around the equator of the capsule and gives rise to a toroidal band of high ρr around the equator which squeezes the hotspot strongly in the r-ϕ (x-y) plane forming two axial jets of hotspot plasma which break out through the weaker confinement of the lower ρr in the axial z direction. The positive P_4 perturbation is representative of the form of perturbation that can arise from, for example, time dependent swings in P_2 or from the capsule support tent. This results in two bands of higher ρr above and below the centre of the hotspot. The symmetry of the convergence of these two bands mean that the very centre of the hotpot is compressed to high pressure within a small radius. A significant fraction of the volume of the hotspot, however, lies outside the region of tight convergence and contributes little to the overall neutron output[33] (see section VI). There are also weak regions of low ρr in the polar and equatorial directions which allow two axial jets and an expanding equatorial ring to form once the hotspot has rebounded and starts to re-expand.

V. GENERATION OF SYNTHETIC NEUTRON DIAGNOSTICS

The principle neutron detectors on NIF which are of interest for this work are: a primary neutron imager of the flux of unscattered DT neutrons emerging from the hotspot; a down scattered neutron imager of the flux of neutrons which scatter in the dense fuel layer surrounding the hotspot and emerge at lower energy[8]; flange Neutron Activation Diagnostics (FNADs)[34,35] which measure the anisotropy in the primary neutron flux due to variations in the ρr of the dense fuel layer in θ and ϕ; and neutron time of flight (nToF) detectors[36,37] which together with the Magnetic Recoil Spectrometer (MRS)[38] measure the energy spectrum of the neutrons which emerge from the capsule.

To generate synthetic neutron diagnostics from the 3D simulation data, we start by constructing source spectra for DD and DT reaction neutrons using an analytic model[12,39], in which we assume that the reactants have a Maxwellian distribution which is shifted due to the bulk motion of the fluid flow. An exact spectrum for the reactants can then be calculated for this distribution in the centre of mass frame, which is then transformed into the lab frame to produce a Doppler broadened and shifted energy spectrum as a function of ion temperature and the angle of emission with respect to the flow vector. For computational expediency, a database of 10^6 spectra is pre-calculated for a range of 100 different ion temperatures, velocity magnitudes and angles. For each computational cell within the hotspot, the ion temperature and velocity are used to determine the source spectrum by interpolating to this database. This process is then repeated, with each cell's contribution, weighted by the product of ion densities, to calculate the total neutron source intensity as a function of energy and emission angles. This provides a calculation of the source spectrum emerging from the hotspot. While this neutron flux is attenuated due to scattering within the dense fuel layer, this does not significantly change the width and shape of the DT neutron spectrum. The effect of scattering on the DD spectrum is likely to be more significant. The results shown below derive the inferred ion temperatures from the unscattered source spectrum. The influence of scattering and additional sources on the shape of the neutron spectra will be subject of future work.

To construct the primary DT neutron images, the attenuation of the flux by scattering in the hotspot and the dense fuel layer is calculated by ray tracing from each source cell in the direction of the detector. Elastic scattering of the neutrons by the background deuterons and tritons is calculated during the ray trace using tabulated energy dependent cross-sections taken from the ENDF database[40]. Synthetic FNADs can then be constructed by integrating the attenuated primary DT neutron spectrum along a given line of sight (LOS). This synthetic diagnostic approach neglects contributions from secondary DT neutron production, reaction in flight neutrons and neutrons scattering into the line of sight. These effects are not thought to provide a major contribution to the structure of images and spectra in the 13-15 MeV range of interest.

Calculation of the down-scattered neutron images and the contributions of scattered neutrons to the overall spectrum is a more intensive computational task. In most previous works, down scattered images have been obtained as a by-product of detailed Monte-Carlo simulations of the total neutron transport within the capsule[41]. This involves modelling the emission from each fusion source as an isotropic particle energy distribution and then following the trajectory of each particle accounting for scattering events, before using the flux emerging from the capsule in the direction of the detector in order to construct an image. The computational expense associated with using this method for 3D radiation hydrodynamic data, normally places constraints on the number of particles that can be calculated and thereby introduces significant numerical noise into synthetic images and spectra. In this work we adopt a different approach which is specifically designed for use in synthetic diagnostics where the detector line of sight is predetermined. The method equates to an inverse ray trace which solves the neutron trajectory backwards in time. From the detector plane, rays are traced back towards the capsule, intersecting with a range of possible scattering sites in the dense fuel and the hotspot. For each scattering site, we survey all of the neutron emitting source cells within the hotspot and use the scattered energy as a function of scattering angle to determine a subset of source cells whose emission will scatter from this site in the direction of the detector and will reach the detector within the desired energy range (here 10-12 MeV).

Having paired the source and scattering cell, the cross section at this scattering angle, along with the density of the scattering cell, is used to calculate the intensity of the source cell emission which is scattered towards the detector as well as the down shift in energy. Attenuation of the neutron flux between the source and scattering cells and between the scattering cell and detector is also calculated. Repeating this process for neutron scattering from both D and T ions for all of the paired scattering sites and source cells, creates a down scattered neutron image at the detector, along with the scattered contributions to the neutron spectrum. The calculation is simplified by assuming that the source spectrum is mono-energetic at 14 MeV. The shape of the scattered spectrum is dominated by the geometric distribution of source cells and scattering sites which produces a statistical range of scattering angles. The scattered spectrum shape is therefore insensitive to the source spectrum. The analysis also assumes that during the neutron transit, the structure of the hotspot and dense fuel layer remain static. This approximation is justified as the unscattered DT and DD neutrons transit the 50μm from the centre of the hotspot to the outer reaches of the fuel in 1.0 ps and 2.3 ps respectively which is much faster than the characteristic burn duration of ~150 ps.

At present this approach is limited to the detection of neutrons undergoing a single scatter event. This approximation is most accurate above 10 MeV, where the intensity of scattered neutrons is highest. For neutron energies below 10MeV, multiple scattering of neutrons and other sources such as TT reactions and deuteron break-up become significant and makes the analysis more complex. These contributions to synthetic neutron diagnostics will be the subject of future work. For these reasons the down scattered images presented here simplify the analysis by covering the the 10-12 MeV range.

In this work, synthetic images and spectra are generated every 25ps during the burn phase in order to assess the contributions of time dependent hotspot and dense fuel structures to time integrated images and spectra.

VI. SYNTHETIC NEUTRON DIAGNOSTICS FOR LOW MODE RADIATION DRIVE ASYMMETRIES

Figure 4, Figure 5 and Figure 6 show synthetic neutron diagnostics for the P_1, P_2 and P_4 perturbations at peak neutron output. In each figure, the image in the right hand column, middle row, is a density slice. Arranged around the density slice are 3 primary DT neutron images in the 13-15MeV range, positioned to show that they are viewing the capsule from above (+z), the side (+x) and below (-z). Positioned outside the primary images are 3 down scattered images in the 10-12 MeV range. Also shown are the DT spectra at peak emission from detectors above, to the side and below, together with the spectrum evaluated with the fluid velocity set to zero, i.e. the spectrum due to purely thermal motion of the ions. Finally the bottom left hand corner shows the ion temperatures inferred from the width of these DT spectra as functions of time. For the P_1 perturbation in Figure 4, the 60 keV up shift in the position of the peak in the DT spectrum observed from below is indicative of a 110 km/s centre of mass velocity moving parallel to the detector direction. This is not however representative of the fluid flow within the simulation where the central jet drives the hotspot material on axis downwards at speeds of 500-800 km/s. This region is however surrounded by a larger volume toroidal region of backflow moving upwards at 100 km/s. The result of the spread or variance of fluid velocities is an extremely broad spectrum width observed in the vertical direction compared to the horizontal observation (which closely matches the neutron spectrum where the fluid motion has not been included). If one were to attribute the widths of time integrated spectra to the Doppler width from a purely thermal ion temperature, this would give a strongly anisotropic result, with the spectra parallel and anti-parallel to the flow giving inferred ion temperatures of 5.43 keV and 5.63 keV and the detector perpendicular to the flow giving 2.86 keV (which is close to the 2.72 keV obtained by setting the fluid velocity to zero). Note that the v=0 inferred ion temperature in Figure 4 follows a similar time dependence to the unperturbed (P_0) calculation, gradually decreasing in time as thermal conduction, radiation and expansion cool the hotspot. The contribution of fluid velocity to the inferred ion temperature is finite in the perpendicular (+x) direction prior to peak compression, but negligible once the principle radial momentum of the implosion has been dissipated in this direction. In the vertical direction however the contribution of fluid velocity to the inferred ion temperature remains significant throughout the pulse. Early in time this is due to the imbalance in momentum from one side of the dense fuel to the other giving rise to centre of mass velocity in the hotpot. Later in time the high pressure of the hotspot cannot be confined by the low ρr of the dense fuel below it and the hotspot breaks out into the residual ablator. At the time of peak neutron output, the regions of highest ion temperature and most intense emission are the on axis regions moving downwards at high speed. The spectrum detected from the –z direction thus sees a stronger weighting where there is a positive Doppler shift than at lower energies (the converse is true for the detector in the +z direction). This bias introduces skewness to the spectra detected parallel and antiparallel to the flow which are no longer well represented by a symmetric Gaussian profile.

The widths of the DD spectra follow a similar time dependence to those for the DT spectra but are systematically narrower. The ratio of the DT to DD spectra widths is sensitive both to the distribution of ion temperatures and to the Doppler broadening caused by fluid flow. The difference in temperature dependence is due to the steeper slope of the DT cross-section versus temperature compared to that for DD. The DT spectrum is therefore more heavily weighted by the higher temperature regions. The higher velocity of DT neutrons in the centre of mass frame means that the absolute increase in energy due to the addition of fluid velocity is larger than for DD. Fluid flow therefore has a stronger influence on the width and shape of the DT spectrum than on the DD spectrum. For the P_1 case, using the inferred temperature as a measure of time integrated DD spectrum width gives 4.40 and 4.67 keV parallel and anti-parallel to the flow compared to 2.58 keV perpendicular to the flow and 2.46 keV with the fluid velocity set to zero. In other words, the DT spectra are much wider along the flow axis than the DD spectra, inferring temperatures roughly 1keV higher, which can be largely attributed to the greater sensitivity of DT spectra to fluid flow since the v=0 cases indicate only a 170eV difference due to the ion temperature distribution.

The primary (13-15 MeV) neutron images replicate the shape of the hotspot (as observed along an integrated line of sight to each detector) with the primary image above showing a significant attenuation due to down scatter in the high ρr of dense fuel above the hotspot. The down scattered images reflect the shape of the dense fuel region and are dominated by the large central jet of dense fuel moving downwards which provides a strong scattering source particularly for neutrons emerging from the hotspot in the vertical direction.

For the P2 perturbation shown in Figure 5, the higher intensity of the radiation around the equator means that this region of the capsule reaches the axis before the polar regions and has a higher ρr in the dense fuel layer. As a consequence, after stagnation, the hotspot is strongly confined in the equatorial directions but is able to break out in the polar directions to form two opposing high velocity jets with outflow velocities of +/- 600 km/s. The velocity variance in these outflows can be observed as significant broadening of the neutron spectrum in the polar direction at peak output and are reflected in the anisotropy of the inferred T_{ion} from time integrated DT spectra which indicate 6.46 keV in end-on, polar (+z and -z) detectors and 3.19 keV in the side on, equatorial (+x) detector compared to 2.95 keV with velocity set to zero. These figures, however, underestimate the instantaneous contributions of flow velocities as indicated from the inferred T_{ion} versus time which shows significant velocity variance in the equatorial direction before peak compression, followed by far higher velocity variance in the polar direction after peak compression. Similarly to the P_1 case, the DD spectra widths follow the DT widths but with reduced sensitivity to the outflow velocity in the vertical direction. The time integrated DD spectra suggest inferred ion temperatures of 5.13 keV along the flow direction and 2.85 keV perpendicular (compared to 2.66 keV with velocities set to zero). Much of the difference in DT and DD spectra widths observed along the flows is due to the large outflow velocities which occur after peak compression. The ion temperatures inferred from the DT spectra are 15% higher than those inferred by the DD spectra during the rising part of the neutron pulse, but this increases to a 35% during the fall of the neutron pulse.

The primary images are dominated by an intense region of neutron emission centred inside the toroidal band of strong convergence around the equatorial direction. Whilst there is minimal attenuation of this flux in the polar directions, the side-on primary image is of lower intensity both due to attenuation of the flux by scattering in the high ρr band of dense fuel and due to the aspect ratio of the source. These scattering events are then the principle source for the side-on down scattered image. The end-on down scattered images provide a good illustration that the detector plane, scatter site and source region are not co-aligned along the same line of sight (LOS). The flux of neutrons reaching the detector plane with energies in the range 10-12 MeV is dominated by neutrons which have been down shifted in energy by undergoing a single scatter through an angle between 60 and 30 degrees[40,6]. In this case, the end-on down scattered images are largely comprised of neutrons which emerge from the central hotspot at an angle to the vertical such that they reach the dense fuel layer surrounding the equator where they then undergo scattering and are redirected towards the end-on detectors. For spherically symmetric results, the ratio of the integrated scattered neutron emission in the 10-12 MeV range to the primary neutron emission in the 13-15 MeV range along a given LOS provides an estimate of the down scattered ratio (DSR) which can be related to the ρr of the dense fuel. For asymmetric results such as in the P_2, this correlation is broken by the lack of alignment between source, scatter site and detector. Comparing the integrated intensity of the down scattered and primary images in Figure 5 produces very similar results in the end-on (2.7%) and side-on (2.8%) directions. Using a value[6] of $\rho r = DSR_{10\text{-}12MeV} * 188\ kg/m^2$, implies a symmetric ρr value of ~5 kg/m^2. Whilst this value approximately matches the average ρr, it does not reflect the very strong asymmetry apparent in the actual ρr of the fuel between the end-on (2.4 kg/m^2) and side-on (9.9 kg/m^2) directions.

In the P_4 perturbation case shown in Figure 6, the hotspot is compressed by two bands of dense fuel above and below the equator. Despite the large amplitude, the symmetry of this perturbation means that the flows still converge accurately upon the imposed axis of symmetry. As a consequence the neutron emission at peak output is dominated by a small central region at the focal point of the two imploding bands of dense fuel which is roughly half the size of the hotspot obtained without a perturbation but which reaches almost as high (76%) a peak pressure. By contrast, the majority of the volume of hotspot material inside the 1keV contour emits only a low intensity neutron flux. The low ρr in both the polar and equatorial directions provides escape paths for outflows after peak compression in the form of axial jets and an expanding toroidal ring. The neutron emission from the regions of the hotspot involved in these outflows is however smaller than that of the central region of the hotspot. The T_{ion} inferred from time resolved DT spectra indicates a finite contribution from the variances in velocity of the polar and equatorial flows during the final stages of implosion but limited contributions from the outflows that occur after peak compression. As a consequence the T_{ion} inferred from time integrated DT spectra is fairly isotropic (3.39 keV end-on and 3.44 keV side-on) and has a relatively small contribution from velocity when compared to the case where velocity is set to zero (2.99 keV). Similarly the DD spectra are also fairly isotropic with the T_{ion} inferred from time integrated spectra being 2.97 keV end-on and 3.02 keV side-on compared to 2.83 keV with velocity set to zero. The difference between DT and DD spectra widths is therefore much reduced compared to that caused by the unidirectional flows in the P1 and P2 examples above and is only marginally higher than the difference due to ion temperature distributions alone.

The primary images for the P_4 case are again dominated by the small region of intense neutron emission at the centre of the hotspot and experience little attenuation due to the low ρr in both the side-on and end-on directions. The down scattered images are dominated by the two circular bands of high ρr in the dense fuel above and below the equator, which scatter neutrons emitted isotropically from within the intense central source region into the end-on and side-on LOS.

VII. MULTI MODE ASYMMETRIES

In the P_1 and P_2 low mode asymmetries described above, the contribution of the flow velocity to the shift, broadening and skew of the neutron spectrum is due to coherent flows of the hotspot material, parallel and anti-parallel along a common axis. The anisotropy in the spectrum shape is due to anisotropic variance of the magnitude of these unidirectional flows rather than changes in their direction. At the other end of the perturbation scale, high mode asymmetries in the hotspot can arise from capsule defects which grow through the Richtmeyer-Meshkov and Rayleigh-Taylor instabilities during ablation and implosion phases. These perturbations may eventually feed through the residual ablator to imprint upon the dense fuel before being further amplified by Rayleigh-Taylor growth during the deceleration phase. Such perturbations introduce multiple incoherent, randomly oriented flows into the hotspot material. In the short wavelength limit, such flows can be approximated as an introduction of a turbulent velocity field to the hotspot[13]. The contribution of the isotropic variance in fluid velocity associated with truly turbulent flow to the width of the DT or DD neutron spectra is almost indistinguishable to that of ion thermal motion, since isotropic motion introduces only very small spectral shifts. The different changes in DT and DD neutron energies caused by each Doppler shift, however, mean that the DT spectrum is broadened more by velocity effects than the DD spectrum and implies that the presence of an isotropic velocity variance can in principle be inferred from a comparison of DT and DD widths[13].

In order to introduce a broad bandwidth of high mode perturbations to the hotspot, we adopt the perturbation structure developed by Taylor et al[3]. Using the same set of initial conditions used for the P_0 calculation, starting at peak implosion velocity, a series of geodesic spheres based on triangular subdivision of an icosahedron are mapped onto the surface of the capsule (21 µm outside of the material interface) in order to determine the locations for Rayleigh-Taylor perturbations. In this case we are interested in high mode behaviour and so have eliminated the lowest order (12 vertices) perturbation. There are then four levels of perturbation remaining using 42, 162, 642 and 2562 points uniformly distributed over the sphere. A total of 3408 perturbations are thus applied by imposing the velocity field of a single Rayleigh-Taylor bubble[42] at each vertex. Each perturbation is assigned a random magnitude, width and direction. Figure 7 illustrates the structure arising from the superposition of different wavelength perturbations on the different geodesic grids at 250 ps after the time that the implosion phase is initialised as well as during the implosion and stagnation phases. Figure 8 shows density slices during the burn phase. The introduction of multiple irregular perturbations introduces non-uniformity to the ρr of the dense fuel layer and its velocity magnitude and direction. The inertia required to confine the hotspot does not arrive simultaneously at all points on the hotspot surface. Non-radial components of the momentum are not extinguished and regions of higher than average radial momentum are not fully decelerated but continue to penetrate into the hotspot. Mix of cold fuel into the hotspot, enhanced thermal conduction losses due to the increased surface area of hotspot[3] and outflow of hotspot material through weak points in ρr, all contribute to truncation of the burn and reduce the yield to 43% of the P_0 case. The velocity slices in Figure 8 show that throughout the burn phase, the hotspot has multiple small scale (10-20 µm) features which are moving at a significant fraction of the implosion velocity and which have different characteristic temperatures.

The widths of the time resolved DT and DD neutron spectra remain largely isotropic until after peak output when the longer wavelength structures contributing to non-uniform breakout of the hotspot introduce some anisotropy. Comparing the T_{ion} inferred from time integrated spectra in three orthogonal directions gives 3.89±0.08 keV for the DT spectra (compared to 3.58 keV with velocities set to zero) and 3.40±0.06 keV for the DD spectra (compared to 3.16 keV with velocities set to zero). Thus the widths of the time integrated DT and DD neutron spectra are almost isotropic and there is a difference in their effective widths (490 eV) which is larger than the level of anisotropy. This difference is however only marginally larger than the 420 eV difference that is observed with the velocities set to zero. It is unlikely therefore that the differences in observable DT and DD neutron spectra widths could be used to infer the presence of the form of velocity in the hotspot induced by this particular type of perturbation scenario.

The limited scattering of the primary neutron flux (here DSRs are 2.9-3.5%) mean that the primary neutron images reflect a volume integration of the neutron emissivity and approximately reproduce the shape of the ion temperature contours. It is tempting to interpret the down scattered images as indicative of the cold fuel structure being backlit by a point source of primary neutrons. The indirect scattering LOS and the distributed primary source however mean that the down scattered images cannot be directly related to the areal density of the dense fuel lying between the hotspot and the detector. For unperturbed P_0 calculations, where the dense fuel is concentrated in a thin hollow sphere, the 60-30º scattering angle undergone by neutrons reaching the detector with 10-12MeV energies produces hollow, circular, down scattered images. The broken up structure of the dense fuel layer in the multi-mode calculations, however, means that the images no longer appear hollow. Instead it is the strongly localised concentrations in ρr (by factors of 2 above the average) which lie off axis from the line of sight, which dominate the down scattered images. In particular, where the dense fuel mixes with the hotspot through the deceleration phase Rayleigh-Taylor instability, jets of cold dense fuel penetrate into the hotspot. These jets provide dense scatter sites which are immersed in and surrounded by intense primary neutron emission regions and therefore provide localised points of relatively intense scattered neutron emission. It should also be noted that ~20% of the neutrons comprising the 10-12 MeV image undergo scattering within the hotspot (T_{ion} > 1 keV) before reaching the dense fuel layer, which further reduces the correlation between the down scattered images and the ρr of the dense fuel.

Despite the significant residual velocity in the hotspot and fuel during the burn phase, the structure of the down scattered images remain fairly constant, changing in intensity with the amplitude of the primary flux. Thus whilst the ~20 μm scale features are at the limit of the range of spatial resolution of the current generation of neutron imaging diagnostics[8,9] on NIF, the temporal blur is not substantial and such structures may become resolvable in time integrated images given further spatial resolution improvements.

The difficulty in extracting data on the fine scale structure of the ρR of the fuel from the neutron diagnostics is further illustrated in Figure 9, which shows maps over the 4π sky of ρR, the FNAD signal and the DSR, at the time of peak neutron emission. Here the ρr is taken from a radial integral of the DT density from the geometric centre of the computational grid, the FNAD is the attenuated primary neutron flux (normalised to the un-attenuated value) and the DSR is the ratio of the scattered (10-12 MeV) flux to the attenuated primary flux. The sky maps are constructed by generating 4535 separate primary and down scattered images, uniformly distributed in θ and ϕ. Whilst both the FNADs and the DSR reflect the average low mode asymmetry of the ρr map (which is dominated by the cluster of high ρr regions near the south pole), the finer scale features of the multi-mode perturbation are not resolved. In the case of the FNADs, this is due to the spatially distributed nature of the neutron source, which limits the spatial resolution compared to a case where all of the emission comes from a point source on axis. In the DSR map, it is the proximity of high ρr scatter points within 30-60º of the line of sight which determines the local intensity of down scattered neutrons rather than the radial integral of ρR.

VIII. DISCUSSION

The difficulty in distinguishing the broadening of neutron spectra due to ion thermal motion from that due to fluid velocity has led to a number of different approaches to unfolding the true ion temperature from the neutron data. One approach is to compare the widths of the DT and DD spectra. For an isothermal hotspot, a greater T_{ion} inferred from the DT spectrum width compared to that from the DD spectrum can be interpreted as a clear indication of variance in the fluid velocity.

In the absence of large scale anisotropy, the velocity variance can be attributed to short scale length motion within the hotspot[13]. The forms of hotspot velocities shown in the previous section, however, suggest that where the hotspot is not isothermal, the effects of the spatial and temporal distribution of ion temperature can be as significant as that due to fluid motion. Another approach is to compare the absolute yields of neutrons from DT reactions to those from the ^{3}He branch of the DD reaction, which is a known ratio as a function of ion temperature and is insensitive to the fluid velocity[43].

Neutron data from 'High-Foot' radiation pulse experiments on NIF are characterised by isotropic spectra widths, with the T_{ion} inferred from DT spectra widths typically higher than that inferred from DD spectra and with a DT to DD yield ratio that is lower than expected for the inferred ion temperatures. The macroscopic bulk fluid flows illustrated by the P_1 and P_2 perturbations in section VI are responsible for considerable broadening of the neutron spectra with the T_{ion} inferred from the DT spectra more than 1 keV higher than that inferred from the DD spectra and ~3 keV higher than the true ion temperatures. The absence of strong anisotropy in the NIF data, however, would appear to indicate either that the implosions are not dominated by such low mode asymmetries, or that if such asymmetries exist, they are not aligned with the axes of the existing nTOF and MRS detectors. Another possibility is the low mode P_2 perturbation due to time dependent radiation drive asymmetry which arises from cross-beam energy transfer in the hohlraum. Such a perturbation causes the capsule to swing from a prolate to oblate P_2 during the final stages of compression and could potentially retain a significant fluid flow whilst producing a time integrated spectrum where the combined effects appear isotropic.

The form and the amplitude of the multi-mode perturbations applied in section VII are largely arbitrary, but are designed to provide an indication of the form of velocity field in the hotspot that might be expected from the feed through of instabilities which grow initially on the outside of the capsule. Table 1 summarises results from a series of runs in which the spatial distribution of the multi-mode perturbation is kept constant, but the magnitude of the initial perturbed component of the velocity is increased. Not surprisingly, higher perturbation amplitudes lead to reduced hotspot confinement, lower hotspot temperatures and a reduced yield due to earlier truncation of the burn[2]. In each case, the minimum value of the kinetic energy of the DT is a small fraction of the maximum value of 8.6-9 kJ which is reached just before stagnation. For strongly perturbed implosions, however, burn truncation can begin ~100 ps prior to this minimum energy point and the residual kinetic energy at peak neutron emission (as shown in the table) is a significant fraction of the implosion kinetic energy. The presence of increasingly large velocities in the hotspot for larger perturbation amplitudes means that the ion temperatures inferred from the DT and DD neutron spectra do not decrease as rapidly as the temperatures inferred when velocities are set to zero. The differences between the inferred temperatures with and without velocity effects become increasingly large with increasing perturbation, reaching 780 eV for the DT spectra. Without the contributions of velocity to the spectra, the T_{ion} for DT remains around 13% higher than that for DD and so the differences in temperature fall along with their decreasing magnitude as the perturbation increases. With the velocity effects included, however, the DT T_{ion} remains ~490 eV higher than the DD T_{ion}, despite the decreasing temperatures, consistent with an increasing velocity contribution at higher perturbation amplitudes. For each of the four cases, the DT to DD yield ratio obtained from the 3D radiation hydrodynamics simulations remains consistent with the T_{ion} inferred from the DT spectra with velocity set to zero. The increasing contribution of fluid velocity to the widths of the neutron spectra at larger perturbation levels, results in an increasing disparity between the temperatures inferred and the temperature implied by the yield ratio.

Whilst these results are qualitatively similar to the trends observed on NIF, it should be noted that increasing the perturbation such that these effects become significant causes the yield to drop well below observed levels. The perturbation method used in section VII induces velocity in the hotspot by feedthrough of instability growth originating in the ablator, but cannot induce significant flow without strongly perturbing the dense fuel layer and compromising confinement. It may be that hotspot motion on a smaller characteristic scale than that induced by these perturbations can retain a strong velocity contribution to the neutron spectra without having such a strong impact on confinement, but it is difficult to envision a driving mechanism for such a perturbation.

A complete analysis of neutron spectra from experiments on NIF may in practice require some combination of the high mode and low mode effects described here to be considered. Isolating the contribution of different spectral components and identifying the source of perturbation which may be responsible for their origin remains a significant challenge.

Acknowledgments

The authors would like to thank Dr. Johan Frenje and Dr. Maria Gatu-Johnson of the Massachusetts Institute of Technology for many invaluable discussions. The results reported in this paper were obtained using the UK National Supercomputing Service ARCHER and the Imperial College High Performance Computer Cx1. This work was supported by the Engineering and Physical Sciences Research Council through grants EP/K028464/1 and EP/L000237/1 and by AWE Aldermaston.

Table I. Results from perturbation amplitude scan for multi-mode simulations.

Pert. Factor	DT T_{ion}	DT T_{ion} v=0	DD T_{ion}	DD T_{ion} v=0	yield / P_0 yield	n_{DT} / n_{DD}	Residual K.E.
0 (P_0)	4.14	4.09	3.73	3.69	1	280	0 %
1	3.89±0.08	3.58	3.40±0.06	3.16	0.43	264	13%
1.5	3.40±0.24	2.83	2.91±0.16	2.48	0.15	237	28%
2	3.20±0.20	2.42	2.72±0.13	2.14	0.07	220	36%

FIGURES

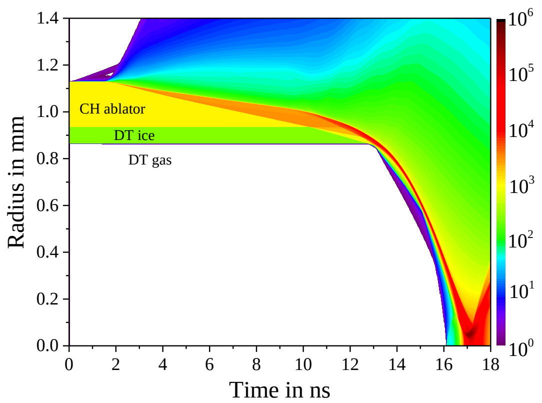

Figure 1. Density (in kg/m^3) as a function of radius and time from a 1D Chimera simulation of N130927 in spherical geometry.

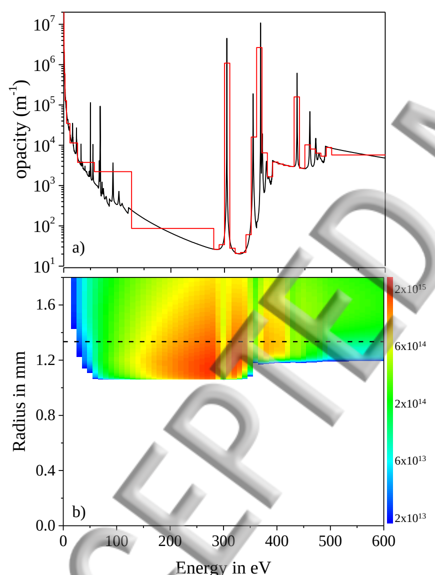

Figure 2. a) Calculated DCA opacities for CH from the Spk code at 10 kg/m^3 and 79 eV corresponding to the ablator at r = 1.33 mm and 6 ns in figure 1, compared to the same opacity data condensed into 38 radiation energy groups. b) Radiative energy flux as a function of energy group and radius, taken from the calculation in figure 1 at 6ns.

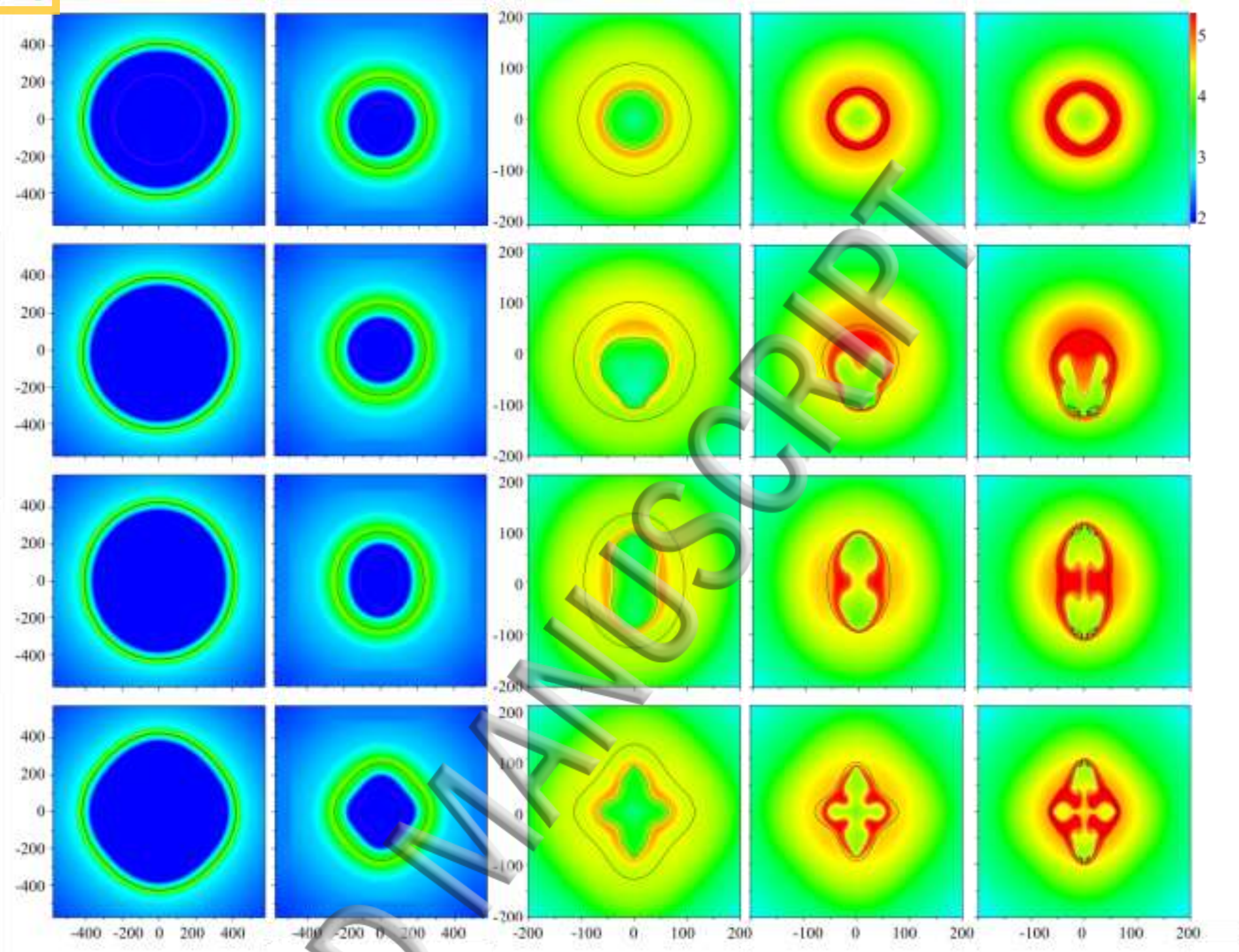

Figure 3. Slices from 3D simulations with P_0, P_1, P_2 and P_4 perturbations, showing contours of $\log_{10}$ of the mass density (in kg/m^3). The black line is the material interface between CH and DT, the violet coloured line is the 1keV T_{ion} contour.

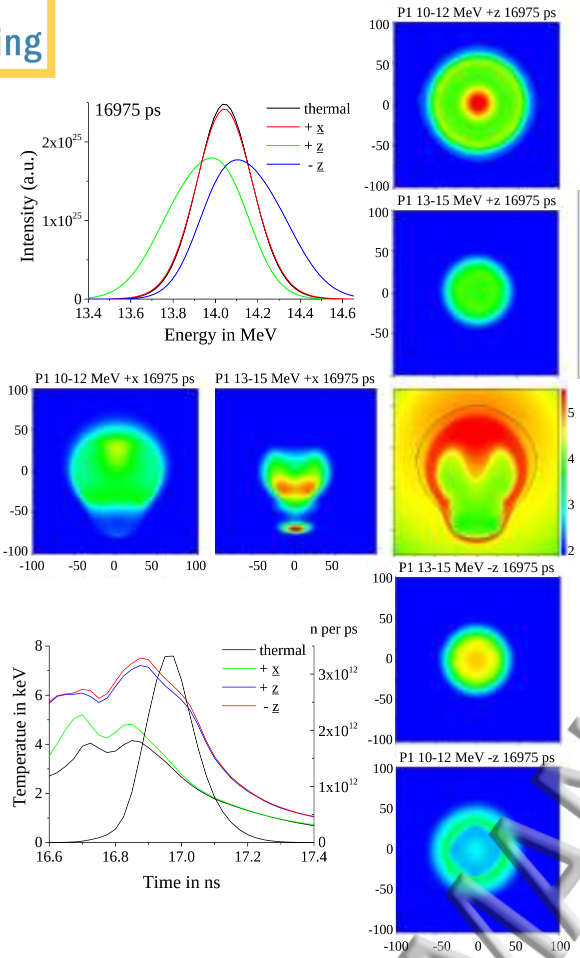

Figure 4. Synthetic neutron diagnostics for a P_1 perturbation at peak output. A density slice is shown in the right hand column, middle row. Primary (13-15MeV) and down scattered (10-12 MeV) DT neutron images are shown as viewed from above (+z), to the side (+x) and below (-z). In the top left corner are the DT spectra at peak output and in the bottom left corner are the time dependent ion temperatures inferred from DT spectra.

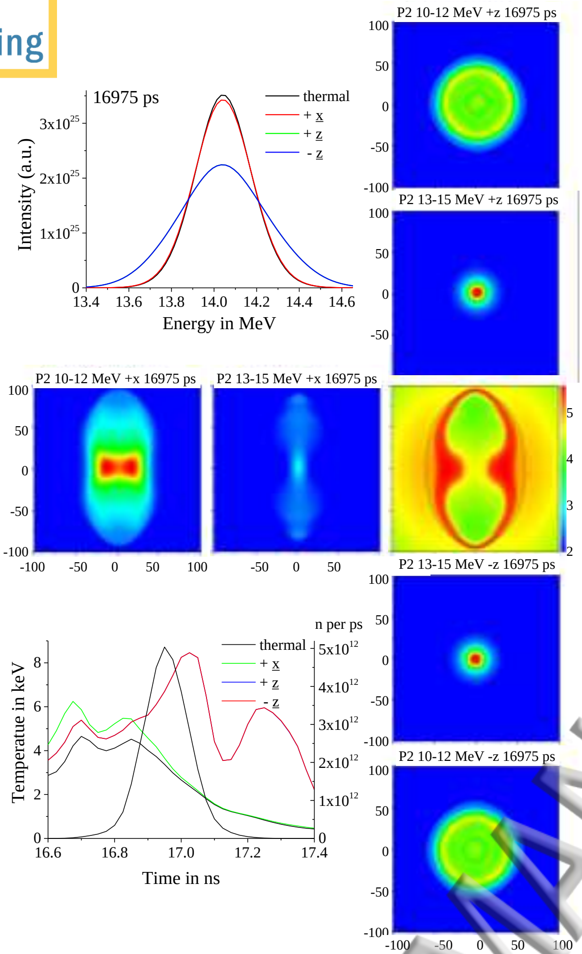

Figure 5. Synthetic neutron diagnostics for a P_2 perturbation at peak output. A density slice is shown in the right hand column, middle row. Primary (13-15MeV) and down scattered (10-12 MeV) DT neutron images are shown as viewed from above (+z), to the side (+x) and below (-z). In the top left corner are the DT spectra at peak output and in the bottom left corner are the time dependent ion temperatures inferred from DT spectra.

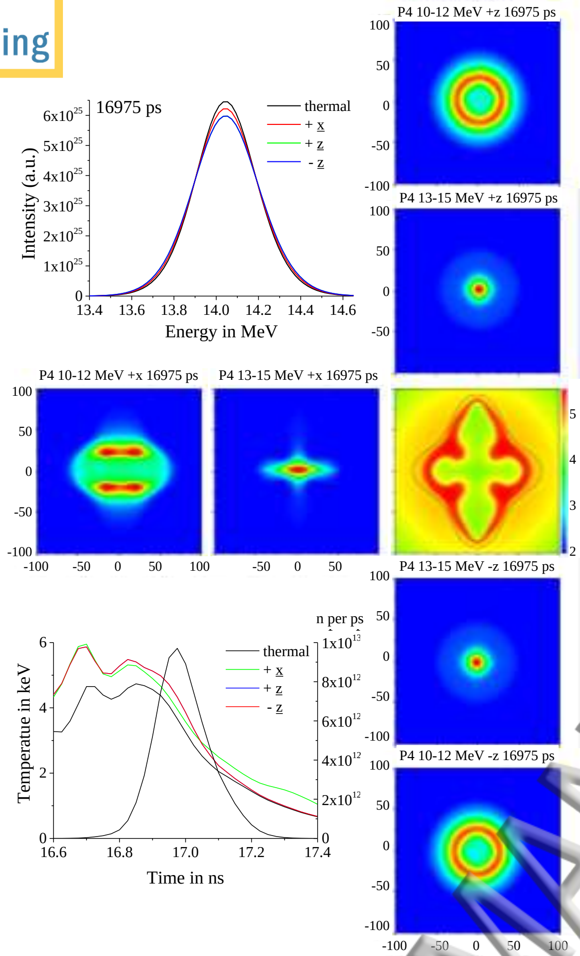

Figure 6. Synthetic neutron diagnostics for a P_4 perturbation at peak output. A density slice is shown in the right hand column, middle row. Primary (13-15MeV) and down scattered (10-12 MeV) DT neutron images are shown as viewed from above (+z), to the side (+x) and below (-z). In the top left corner are the DT spectra at peak output and in the bottom left corner are the time dependent ion temperatures inferred from DT spectra.

Figure 7. Constant density surfaces at 2500 kg/m^3 from a multi-mode calculation at 250 ps after the time that the implosion is initialised, during the implosion and during stagnation

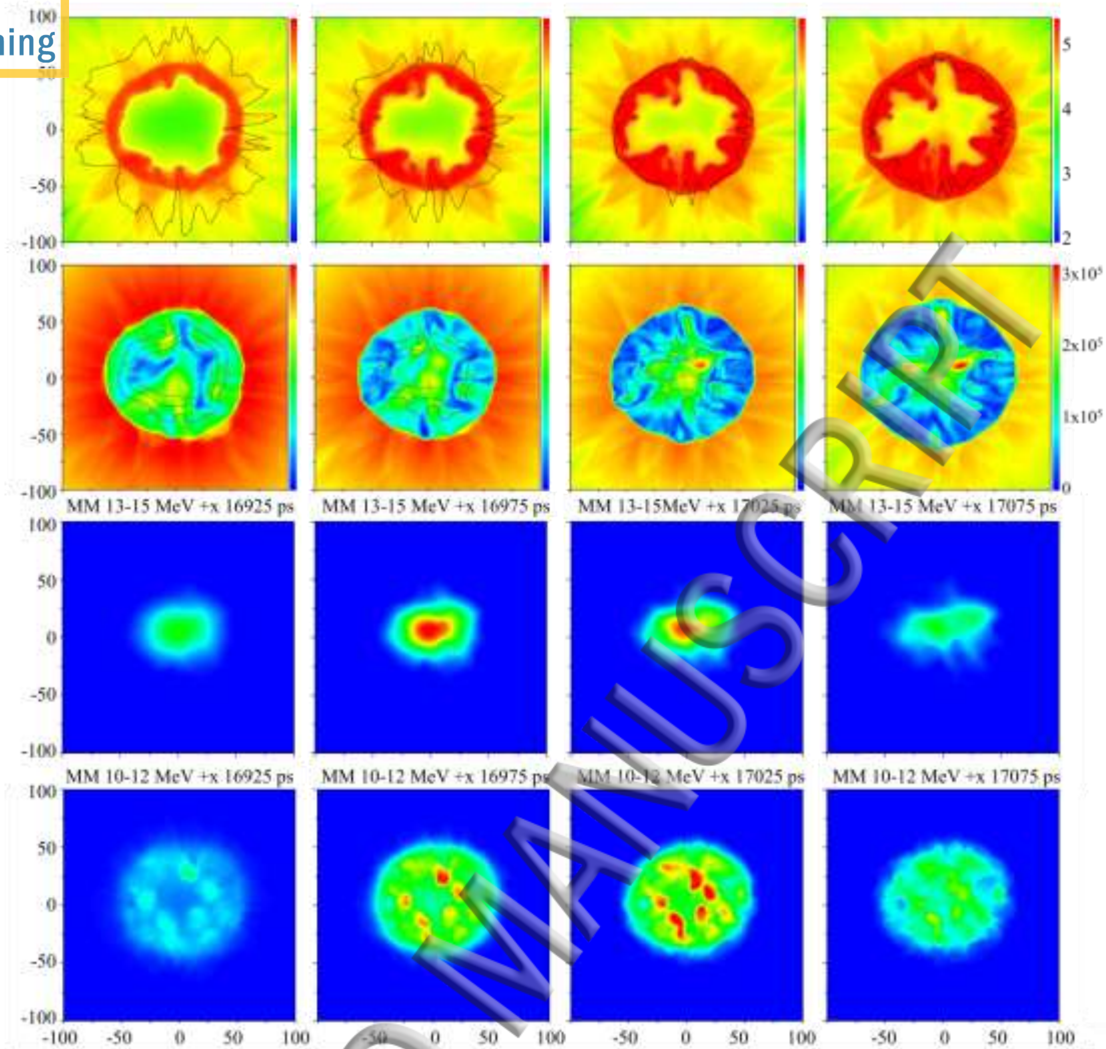

Figure 8. Slices of density and velocity magnitude, together with primary and down scattered neutron images throughout the burn pulse for a multi-mode perturbation. The velocity slices also show ion temperature contours at 1, 3 and 5 keV.

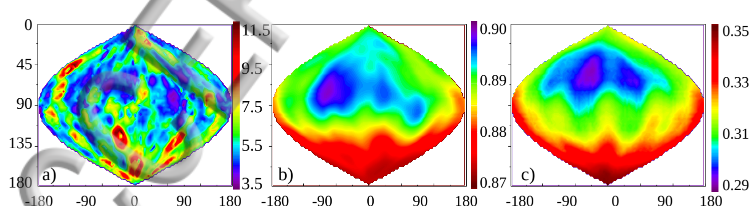

Figure 9. Sky maps of a) the areal density (in kg/m^2), b) the FNAD and c) the DSR. Note that the color scale on the FNAD image has been inverted to facilitate comparison.

References

[1] D. S. Clark , D. E. Hinkel , D. C. Eder , O. S. Jones , S. W. Haan , B. A. Hammel , M. M. Marinak , J. L. Milovich , H. F. Robey , L. J. Suter , and R. P. J. Town , Phys. Plasmas **20**(5), 056318 (2013).

[2] S. Taylor, B. Appelbe, N. P. Niasse and J. P. Chittenden, Proceedings of the 7th International Conference on Inertial Fusion Sciences and Applications, EPJ Web of Conferences **59**, 04009 (2013).

[3] S. Taylor and J. P. Chittenden, Physics of Plasmas **21**, 062701, (2014).

[4] C. R. Weber D. S. Clark, A. W. Cook, D. C. Eder, S. W. Haan, B. A. Hammel, D. E. Hinkel, O. S. Jones, M. M. Marinak, J. L. Milovich, P. K. Patel, H. F. Robey, J. D. Salmonson, S. M. Sepke and C. A. Thomas, Phys. Plasmas **22**, 032702 (2015);

[5] B. K. Spears, D. H. Munro, S. Sepke, J. Caggiano, D. Clark, R. Hatarik, A. Kritcher, D. Sayre, C. Yeamans, J. Knauer, T. Hilsabeck and J. Kilkenny, Phys. Plasmas **22**, 056317 (2015)

[6] M. Gatu Johnson, J. A. Frenje, D. T. Casey, C. K. Li, F. H. Seguin, R. Petrasso, R. Ashabranner, R. M. Bionta, D. L. Bleuel, E. J. Bond, J. A. Caggiano, A. Carpenter, C. J. Cerjan, T. J. Clancy, T. Doeppner, M. J. Eckart, M. J. Edwards, S. Friedrich, S. H. Glenzer, S. W. Haan, E. P. Hartouni, R. Hatarik, S. P. Hatchett, O. S. Jones, G. Kyrala, S. Le Pape, R. A. Lerche, O. L. Landen, T. Ma, A. J. MacKinnon, M. A. McKernan, M. J. Moran, E. Moses, D. H. Munro, J. McNaney, H. S. Park, J. Ralph, B. Remington, J. R. Rygg, S. M. Sepke, V. Smalyuk, B. Spears, P. T. Springer, C. B. Yeamans, M. Farrell, D. Jasion, J. D. Kilkenny, A. Nikroo, R. Paguio, J. P. Knauer, V. Yu Glebov, T. C. Sangster, R. Betti, C. Stoeckl, J. Magoon, M. J. Shoup, G. P. Grim, J. Kline, G. L. Morgan, T. J. Murphy, R. J. Leeper, C. L. Ruiz, G. W. Cooper, and A. J. Nelson, Rev. Sci. Instrum. **83**, 10D308 (2012).

[7] J.A. Frenje R. Bionta, E.J. Bond, J.A. Caggiano, D.T. Casey, C. Cerjan, J. Edwards, M. Eckart2, D.N. Fittinghoff, S. Friedrich, V.Yu. Glebov, S. Glenzer, G. Grim, S. Haan, R. Hatarik, S. Hatchett, M. Gatu Johnson, O.S. Jones, J.D. Kilkenny, J.P. Knauer, O. Landen, R. Leeper, S. Le Pape, R. Lerche, C.K. Li, A. Mackinnon, J. McNaney, F.E. Merrill, M. Moran, D.H. Munro, T.J. Murphy, R.D. Petrasso, R. Rygg, T.C. Sangster, F.H. S´eguin, S. Sepke, B. Spears, P. Springer, C. Stoeckl and D.C. Wilson, Nuclear Fusion **53**, 043014, (2013)

[8] F. E. Merrill, D. Bower, R. Buckles, D. D. Clark, C. R. Danly, O. B. Drury, J. M. Dzenitis, V. E. Fatherley, D. N. Fittinghoff, R. Gallegos, G. P. Grim, N. Guler, E. N. Loomis, S. Lutz, R. M. Malone, D. D. Martinson, D. Mares, D. J. Morley, G. L. Morgan, J. A. Oertel, I. L. Tregillis, P. L. Volegov, P. B. Weiss, C. H. Wilde and D. C. Wilson, Rev. Sci. Instrum., **83**, 10D317 (2012).

[9] G. P. Grim, N. Guler, F. E. Merrill, G. L. Morgan, C. R. Danly, P. L. Volegov, C. H. Wilde, D. C. Wilson, D. S. Clark, D. E. Hinkel, O. S. Jones, K. S. Raman, N. Izumi, D. N. Fittinghoff, O. B. Drury, E. T. Alger, P. A. Arnold, R. C. Ashabranner, L. J. Atherton, M. A. Barrios, S. Batha, P. M. Bell, L. R. Benedetti, R. L. Berger, L. A. Bernstein, L. V. Berzins, R. Betti, S. D. Bhandarkar, R. M. Bionta, D. L. Bleuel, T. R. Boehly, E. J. Bond, M. W. Bowers, D. K. Bradley, G. K. Brunton, R. A. Buckles, S. C. Burkhart, R. F. Burr, J. A. Caggiano, D. A. Callahan, D. T. Casey, C. Castro, P. M. Celliers, C. J. Cerjan, G. A. Chandler, C. Choate, S. J. Cohen, G. W. Collins, G. W. Cooper, J. R. Cox, J. R. Cradick, P. S. Datte, E. L. Dewald, P. Di Nicola, J. M. Di Nicola, L. Divol, S. N. Dixit, R. Dylla-Spears, E. G. Dzenitis, M. J. Eckart, D. C. Eder, D. H. Edgell, M. J. Edwards, J. H. Eggert, R. B. Ehrlich, G. V. Erbert, J. Fair, D. R. Farley, B. Felker, R. J. Fortner, J. A. Frenje, G. Frieders, S. Friedrich, M. Gatu-Johnson, C. R. Gibson, E. Giraldez, V. Y. Glebov, S. M. Glenn, S. H. Glenzer, G. Gururangan, S. W. Haan, K. D. Hahn, B. A. Hammel, A. V. Hamza, E. P. Hartouni, R. Hatarik, S. P. Hatchett, C. Haynam, M. R. Hermann, H. W. Herrmann, D. G. Hicks, J. P. Holder, D. M. Holunga, J. B. Horner, W. W. Hsing, H. Huang, M. C. Jackson, K. S. Jancaitis,

D. H. Kalantar, R. L. Kauffman, M. I. Kauffman, S. F. Khan, J. D. Kilkenny, J. R. Kimbrough, R. Kirkwood, J. L. Kline, J. P. Knauer, K. M. Knittel, J. A. Koch, T. R. Kohut, B. J. Kozioziemski, K. Krauter, G. W. Krauter, A. L. Kritcher, J. Kroll, G. A. Kyrala, K. N. La Fortune, G. LaCaille, L. J. Lagin, T. A. Land, O. L. Landen, D. W. Larson, D. A. Latray, R. J. Leeper, T. L. Lewis, S. LePape, J. D. Lindl, R. R. Lowe-Webb, T. Ma, B. J. MacGowan, A. J. MacKinnon, A. G. MacPhee, R. M. Malone, T. N. Malsbury, E. Mapoles, C. D. Marshall, D. G. Mathisen, P. McKenty, J. M. McNaney, N. B. Meezan, P. Michel, J. L. Milovich, J. D. Moody, A. S. Moore, M. J. Moran, K. Moreno, E. I. Moses, D. H. Munro, B. R. Nathan, A. J. Nelson, A. Nikroo, R. E. Olson, C. Orth, A. E. Pak, E. S. Palma, T. G. Parham, P. K. Patel, R. W. Patterson, R. D. Petrasso, R. Prasad, J. E. Ralph, S. P. Regan, H. Rinderknecht, H. F. Robey, G. F. Ross, C. L. Ruiz, F. H. Séguin, J. D. Salmonson, T. C. Sangster, J. D. Sater, R. L. Saunders, M. B. Schneider, D. H. Schneider, M. J. Shaw, N. Simanovskaia, B. K. Spears, P. T. Springer, C. Stoeckl, W. Stoeffl, L. J. Suter, C. A. Thomas, R. Tommasini, R. P. Town, A. J. Traille, B. Van Wonterghem, R. J. Wallace, S. Weaver, S. V. Weber, P. J. Wegner, P. K. Whitman, K. Widmann, C. C. Widmayer, R. D. Wood, B. K. Young, R. A. Zacharias and A. Zylstra, Phys. Plasmas **20**, 056320 (2013);

[10] M. Gatu Johnson, D. T. Casey, J. A. Frenje, C.-K. Li, F. H. Seguin, R. D. Petrasso, R. Ashabranner, R. Bionta, S. LePape, M. McKernan, A. Mackinnon, J. D. Kilkenny, J. Knauer, and T. C. Sangster, Phys. Plasmas **20**, 042707 (2013);

[11] B. K. Spears , M. J. Edwards , S. Hatchett , J. Kilkenny , J. Knauer , A. Kritcher , J. Lindl , D. Munro , P. Patel , H. F. Robey , and R. P. J. Town, Phys. Plasmas **21**(4), 042702 (2014).

[12] B Appelbe and J Chittenden, Plasma Phys. Control. Fusion **53,** 045002 (2011).

[13] T. J. Murphy, Phys. Plasmas, **21** p072701 (2014).

[14] D. H. Munro, Nucl. Fusion **56,** 036001 (2016).

[15] B. van Leer, J. Com. Phys., **32**, 101 (1979).

[16] D. L. Youngs, in Numerical Methods for Fluid Dynamics, edited by K. W. Morton and M. J. Baines (Academic Press, New York, 1982).

[17] W. F. Noh, P. Woodward. Proceedings of the Fifth International Conference on Numerical Methods in Fluid Dynamics, 1976, Volume of the series Lecture Notes in Physics **59** 330 (2005).

[18] S. Faik, M. M. Basko, A. Tauschwitz, I. Iosilevskiy, and J. A. Maruhn, High Energy Density Phys. **8**(4), 349–359 (2012).

[19] A. J. Kemp and J. Meyer ter Vehn, Nucl. Instrum. Methods, Phys. Res., Sect. A **415**, 674 (1998).

[20] R. M. More, K. H. Warren, D. A. Young, and G. B. Zimmerman, Phys. Fluids **31**, 3059 (1988).

[21] E. M. Epperlein and M. G. Haines, Phys. Fluids **29**, 1029 (1986).

[22] S.I. Braginskii, Transport Processes in Plasma. Reviews of Plasma Physics, 1, 205. (1965)

[23] C.A. Jennings, PhD thesis, Imperial College, (2005).

[24] G. L. Olson, L. H. Auer, and M. L. Hall, J. Quant. Spectros. Rad. Transf. **64** 619 (1999).

[25] D. Mihalas and R. Weaver, J. Quant. Spectros. Rad. Transf. **28**, 213 (1982).

[26] J. M. Stone, D. Mihalas, and M. L. Norman, Astrophys. J. Supp., **80,** 819 (1992).

[27] N.P. Niasse, PhD thesis, Imperial College, (2011).

[28] G. Faussurier, C. Blancard and P. Renaudin., High Energy Density Physics **4**, 114 (2008).

[29] Kramida, A., Ralchenko, Yu., Reader, J. and NIST ASD Team (2015). NIST Atomic Spectra Database (version 5.3), http://physics.nist.gov/asd (20th Jan. 2016).

[30] M. Busquet, D. Colombant, M. Klapisch, D. Fyfe and J. Gardner, High Energy Density Physics, **5**, 270 (2009)

[31] O. A. Hurricane, D. A. Callahan, D. T. Casey, P. M. Celliers, C. Cerjan, E.L. Dewald, T. R. Dittrich, T. Doeppner, D. E. Hinkel, L. F. Berzak Hopkins, J. L. Kline, S. Le Pape, T. Ma, A. G. MacPhee, J. L. Milovich, A. Pak, H. S. Park, P. K. Patel, B. A. Remington, J. D. Salmonson, P. T.

Springer, and R. Tommasini, Nature **506,** 343 (2014).

[32] H. F. Robey, P. M. Celliers, J. L. Kline, A. J. Mackinnon, T. R. Boehly, O. L. Landen, J. H. Eggert, D. Hicks, S. Le Pape, D. R. Farley, M. W. Bowers, K. G. Krauter, D. H. Munro, O. S. Jones, J. L. Milovich, D. Clark, B. K. Spears, R. P. J. Town, S. W. Haan, S. Dixit, M. B. Schneider, E. L. Dewald, K. Widmann, J. D. Moody, T. Doeppner, H. B. Radousky, A. Nikroo, J. J. Kroll, A. V. Hamza, J. B. Horner, S. D. Bhandarkar, E. Dzenitis, E. Alger, E. Giraldez, C. Castro, K. Moreno, C. Haynam, K. N. LaFortune, C. Widmayer, M. Shaw, K. Jancaitis, T. Parham, D. M. Holunga, C. F. Walters, B. Haid, T. Malsbury, D. Trummer, K. R. Coffee, B. Burr, L. V. Berzins, C. Choate, S. J. Brereton, S. Azevedo, H. Chandrasekaran, S. Glenzer, J. A. Caggiano, J. P. Knauer, J. A. Frenje, D. T. Casey, M. Gatu Johnson, F. H. Seguin, B. K. Young, M. J. Edwards, B. M. Van Wonterghem, J. Kilkenny, B. J. MacGowan, J. Atherton, J. D. Lindl, D. D. Meyerhofer, and E. Moses, Phys. Rev. Lett. **108**, 215004 (2012).

[33] R. H. H. Scott, D. S. Clark, D. K. Bradley, D. A. Callahan, M. J. Edwards, S. W. Haan, O. S. Jones, B. K. Spears, M. M. Marinak, R. P. J. Town, P. A. Norreys, and L. J. Suter, Phys. Rev. Lett. **110**, 075001 (2013).

[34] D. L. Bleuel C. B. Yeamans, L. A. Bernstein, R. M. Bionta, J. A. Caggiano, D. T. Casey, G. W. Cooper, O. B. Drury, J. A. Frenje, C. A. Hagmann, R. Hatarik, J. P. Knauer, M. Gatu Johnson, K. M. Knittel, R. J. Leeper, J. M. McNaney, M. Moran, C. L. Ruiz and D. H. G. Schneider, Rev. Sci. Instrum. **83**, 10D313 (2012).

[35] C. B. Yeamans, D. L. Bleuel and L. A. Bernstein Rev. Sci. Instrum. **83**, 10D315 (2012);

[36] V. Yu. Glebov T. C. Sangster, C. Stoeckl, J. P. Knauer, W. Theobald, K. L. Marshall, M. J. Shoup III, T. Buczek, M. Cruz, T. Duffy, M. Romanofsky, M. Fox, A. Pruyne, M. J. Moran, R. A. Lerche, J. McNaney, J. D. Kilkenny, M. J. Eckart, D. Schneider, D. Munro, W. Stoeffl, R.

Zacharias, J. J. Haslam, T. Clancy, M. Yeoman, D. Warwas, C. J. Horsfield, J.-L. Bourgade, O. Landoas, L. Disdier, G. A. Chandler and R. J. Leeper, Rev. Sci. Instrum. **81**, 10D325 (2010).

[37] R. Hatarik, D. B. Sayre, J. A. Caggiano, T. Phillips, M. J. Eckart, E. J. Bond, C. Cerjan, G. P. Grim, E. P. Hartouni, J. P. Knauer, J. M. Mcnaney and D. H. Munro, J. Appl. Phys. **118**, 184502 (2015).

[38] J. A. Frenje, D. T. Casey, C. K. Li, F. H. Séguin, R. D. Petrasso, V. Yu. Glebov, P. B. Radha, T. C. Sangster, D. D. Meyerhofer, S. P. Hatchett, S. W. Haan, C. J. Cerjan, O. L. Landen, K. A. Fletcher and R. J. Leeper, Phys. Plasmas **17**, 056311 (2010).

[39] B. Appelbe and J. P. Chittenden, High Energy Density Physics **11**, 30, (2014).

[40] M.B. Chadwick, M. Herman, P. Oblo˘zinsk´y, M.E. Dunn, Y. Danon, A.C. Kahler, D.L. Smith, B. Pritychenko, G. Arbanas, R. Arcilla, R. Brewer, D.A. Brown,, R. Capote, A.D. Carlson, Y.S. Cho, H. Derrien, K. Guber, G.M. Hale, S. Hoblit, S. Holloway, T.D. Johnson, T. Kawano, B.C. Kiedrowski, H. Kim, S. Kunieda,, N.M. Larson, L. Leal, J.P. Lestone, R.C. Little, E.A. McCutchan, R.E. MacFarlane, M. MacInnes, C.M. Mattoon, R.D. McKnight, S.F. Mughabghab, G.P.A. Nobre, G. Palmiotti, A. Palumbo, M.T. Pigni, V.G. Pronyaev, R.O. Sayer, A.A. Sonzogni, N.C. Summers, P. Talou, I.J. Thompson, A. Trkov, R.L. Vogt, S.C. van der Marck, A. Wallner, 12 M.C. White, D. Wiarda and P.G. Young, Nuclear Data Sheets, **112**, p. 2887 (2011).

[41] D. C. Wilson, G. P. Grim, I. L. Tregillis, M. D. Wilke, M. V. Patel, S. M. Sepke, G. L. Morgan, R. Hatarik, E. N. Loomis, C. H. Wilde, J. A. Oertel, V. E. Fatherley, D. D. Clark, D. N. Fittinghoff, D. E. Bower, M. J. Schmitt, M. M. Marinak, D. H. Munro, F. E. Merrill, M. J. Moran, T.-S. F. Wang, C. R. Danly, R. A. Hilko, S. H. Batha, M. Frank, and R. Buckles, Rev. Sci. Instrum. **81**, 10D335 (2010).

[42] D. Layzer, Astrophys. J. **122**, 1 (1955).

[43] M. Gatu Johnson, J.P. Knauer, C.J. Cerjan, M.J. Eckart, G.P. Grim, E.P. Hartouni, R. Hatarik, J.D. Kilkenny, D.H. Munro, D.B. Sayre, B.K. Spears, R.M. Bionta, E.J. Bond, J.A. Caggiano, D. Callahan, D.T. Casey, T. Döppner, J.A. Frenje, V.Yu. Glebov, O. Hurricane, A. Kritcher, S. LePape, T. Ma, A. Mackinnon, N. Meezan, P. Patel, R.D. Petrasso, J.E. Ralph, P.T. Springer, and C.B. Yeamans, submitted to Phys. Rev. Lett. (2016).

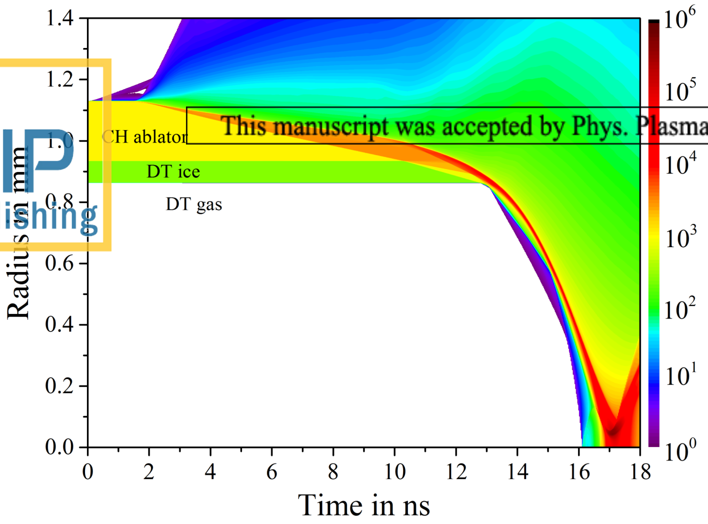

Figure 1. Density (in kg/m^3) as a function of radius and time from a 1D Chimera simulation of N130927 in spherical geometry.

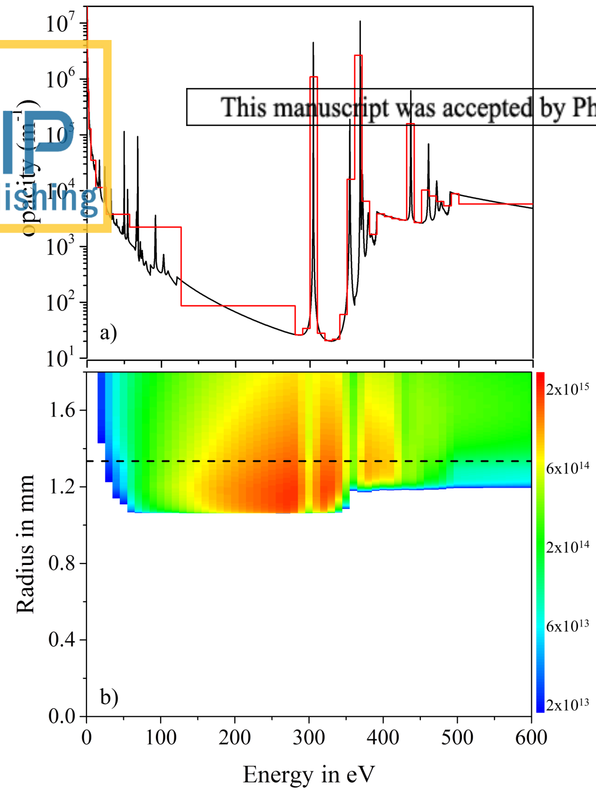

Figure 2. a) Calculated DCA opacities for CH from the Spk code at 10 kg/m^3 and 79 eV corresponding to the ablator at r = 1.33 mm and 6 ns in figure 1, compared to the same opacity data condensed into 38 radiation energy groups. b) Radiative energy flux as a function of energy group and radius, taken from the calculation in figure 1 at 6ns.

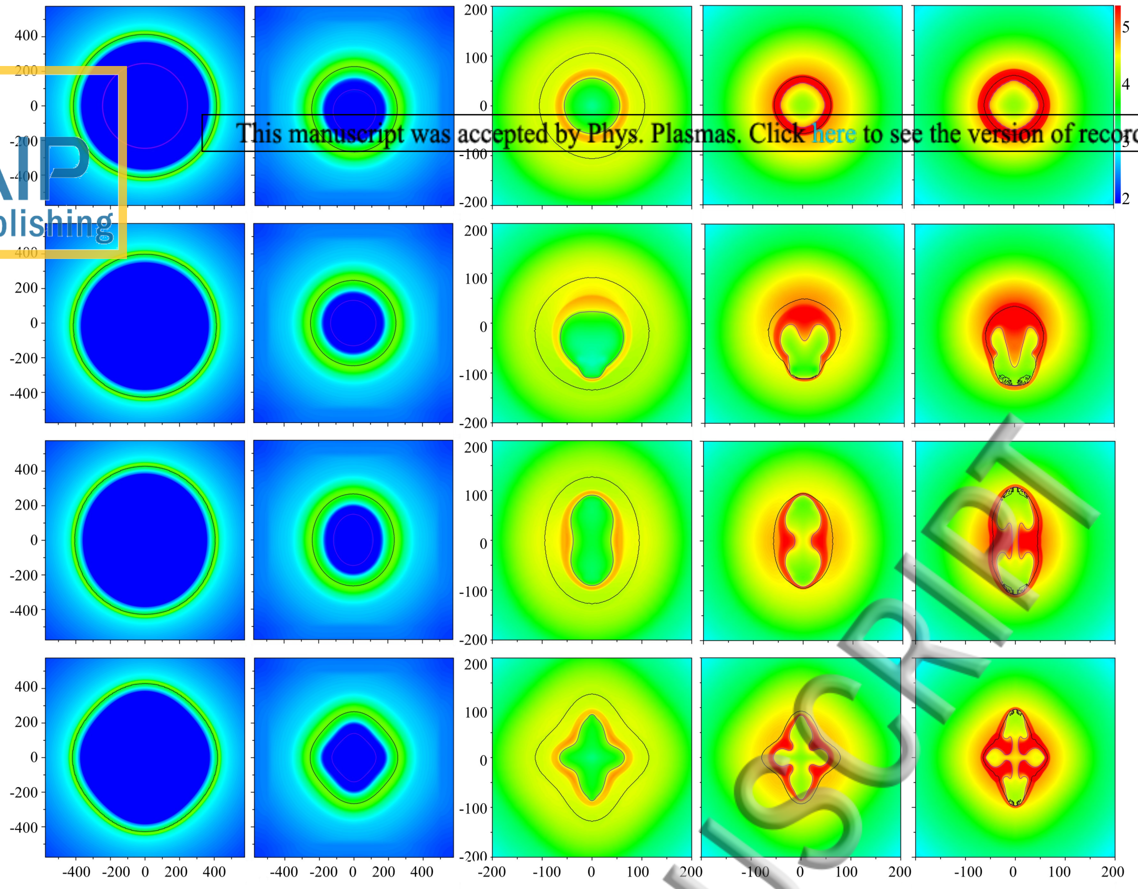

Figure 3. Slices from 3D simulations with P_0, P_1, P_2 and P_4 perturbations, showing contours of $\log_{10}$ of the mass density (in kg/m^3). The black line is the material interface between CH and DT, the violet coloured line is the 1keV T_{ion} contour.

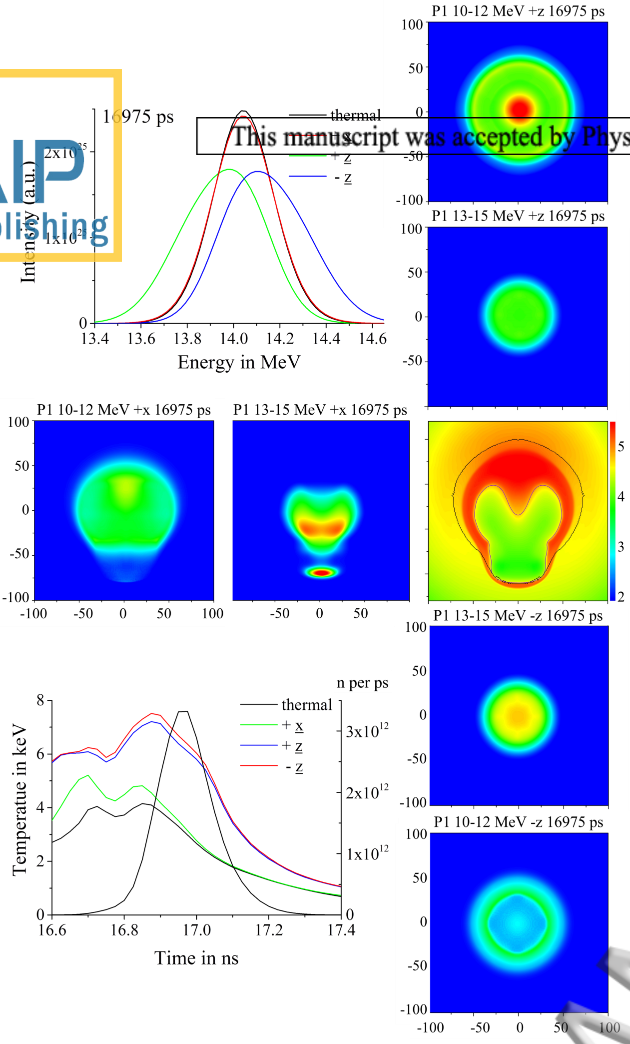

Figure 4. Synthetic neutron diagnostics for a P_1 perturbation at peak output. A density slice is shown in the right hand column, middle row. Primary (13-15MeV) and down scattered (10-12 MeV) DT neutron images are shown as viewed from above (+z), to the side (+x) and below (-z). In the top left corner are the DT spectra at peak output and in the bottom left corner are the time dependent ion temperatures inferred from DT spectra.

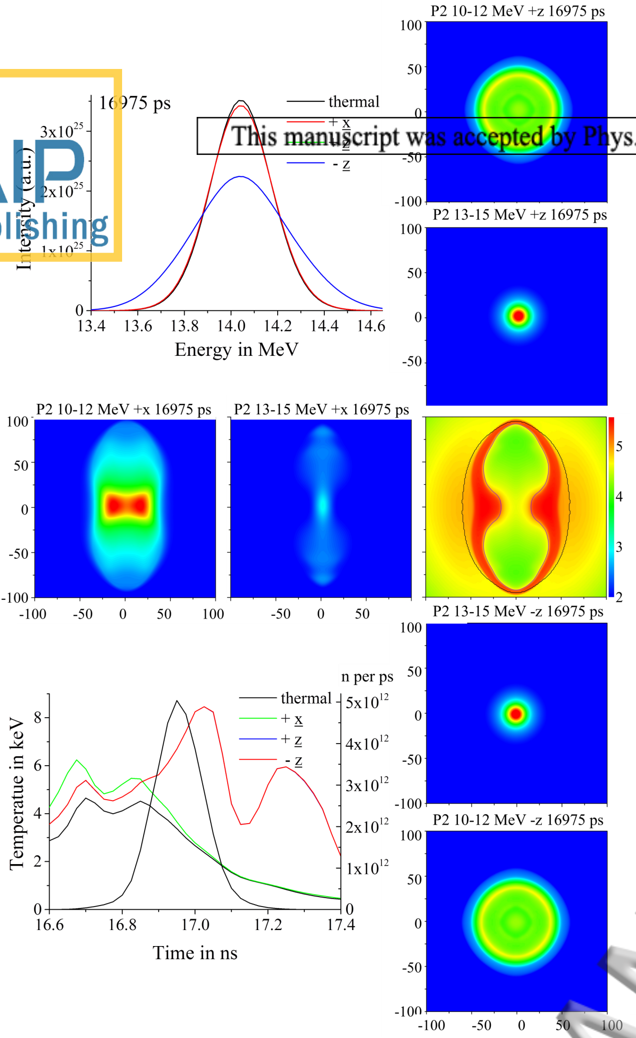

Figure 5. Synthetic neutron diagnostics for a P_2 perturbation at peak output. A density slice is shown in the right hand column, middle row. Primary (13-15MeV) and down scattered (10-12 MeV) DT neutron images are shown as viewed from above (+z), to the side (+x) and below (-z). In the top left corner are the DT spectra at peak output and in the bottom left corner are the time dependent ion temperatures inferred from DT spectra.

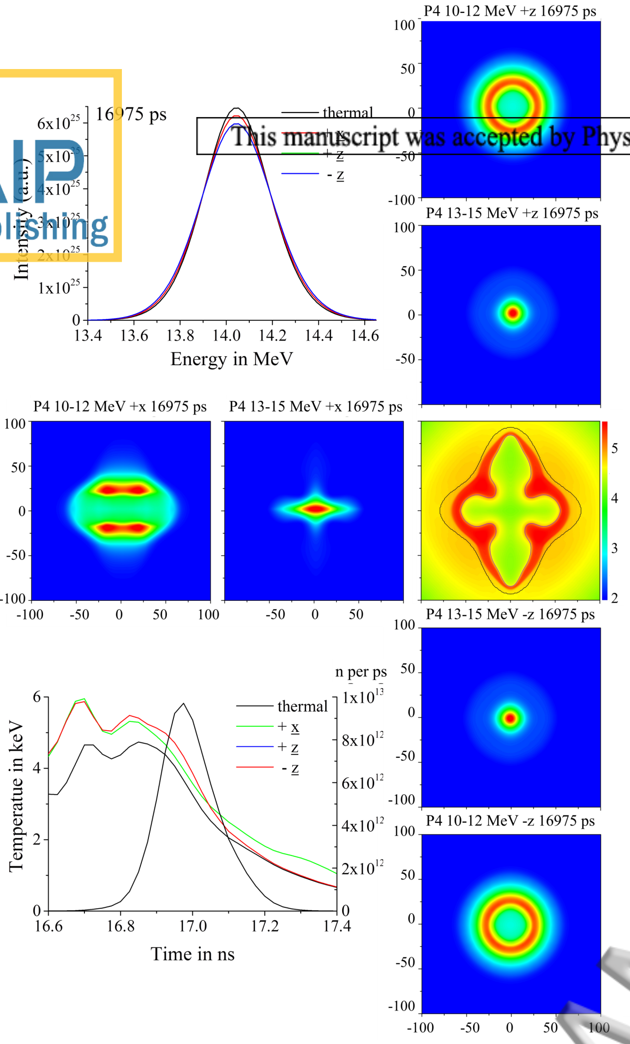

Figure 6. Synthetic neutron diagnostics for a P_4 perturbation at peak output. A density slice is shown in the right hand column, middle row. Primary (13-15MeV) and down scattered (10-12 MeV) DT neutron images are shown as viewed from above (+z), to the side (+x) and below (-z). In the top left corner are the DT spectra at peak output and in the bottom left corner are the time dependent ion temperatures inferred from DT spectra.

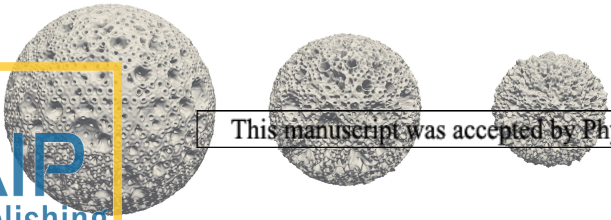

Figure 7. Constant density surfaces at 2500 kg/m^3 from a multi-mode calculation at 250 ps after the time that the implosion is initialised, during the implosion and during stagnation.

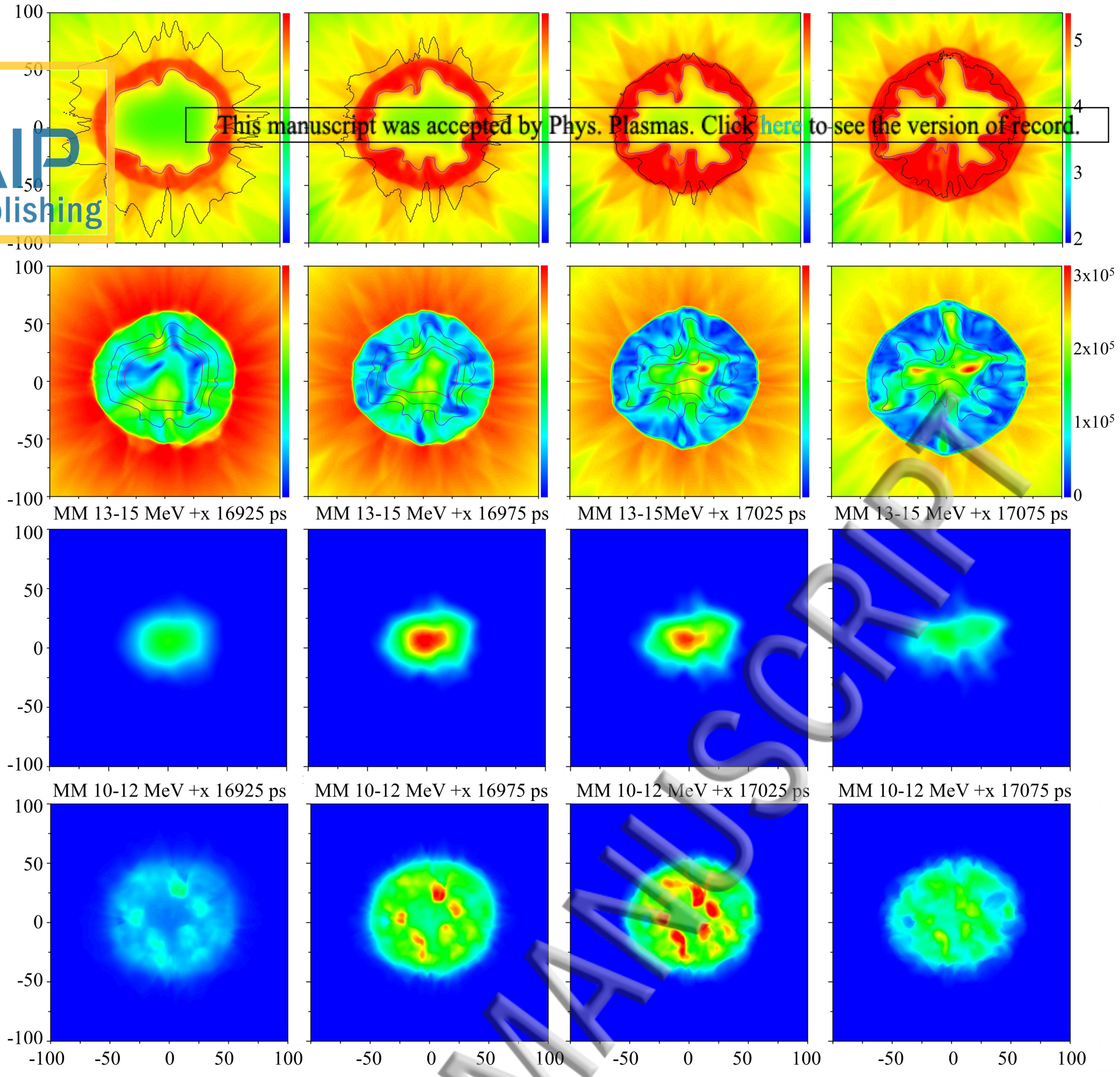

Figure 8. Slices of density and velocity magnitude, together with primary and down scattered neutron images throughout the burn pulse for a multi-mode perturbation. The velocity slices also show ion temperature contours at 1, 3 and 5 keV.

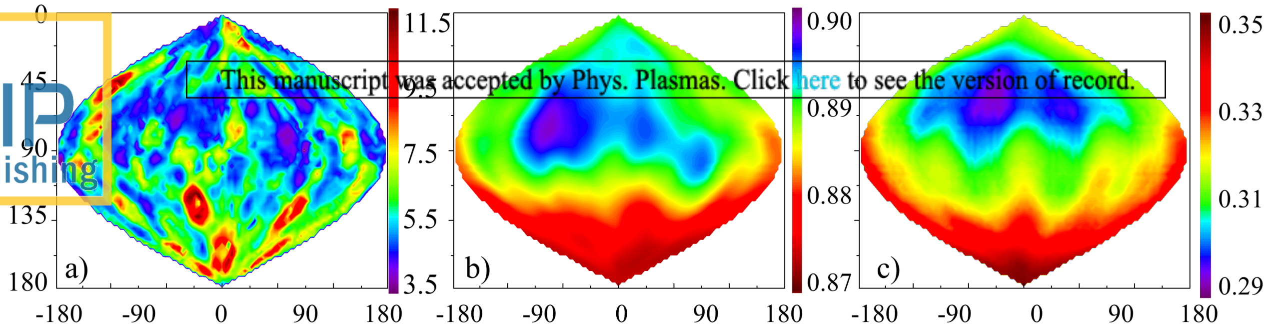

Figure 9. Sky maps of a) the areal density (in kg/m^2), b) the FNAD and c) the DSR. Note that the color scale on the FNAD image has been inverted to facilitate comparison.